

# 1 A daily sunshine duration (SD) dataset in China from 2 Himawari AHI imagery (2016-2023)

3 Zhanhao Zhang<sup>1,2</sup>, Shibo Fang<sup>1</sup>, Jiahao Han<sup>1</sup>

4 <sup>1</sup>State Key Laboratory of Severe Weather, Chinese Academy of Meteorological Sciences, Beijing  
5 100081, China

6 <sup>2</sup>College of Earth and Planetary Sciences, University of Chinese Academy of Sciences, Beijing, 100049,  
7 China

8 *Correspondence to:* Shibo Fang (sbfang0110@163.com)

9  
10 **Abstract.** Monitoring global radiation resources relies on sunshine duration (SD) as a significant  
11 indication, but there is a scarcity of research that have examined high-resolution SD data. This study  
12 established a daily 5-km SD dataset in China from 2016 to 2023 using Himawari's Advanced Himawari  
13 Imager (AHI) Level 3 shortwave radiation fitted with the Ångström-Prescott model based on time series.  
14 We used ground-measured SD at 2380 Chinese Meteorological Administration (CMA) stations to verify  
15 the accuracy of SD dataset. The results of the testing set indicated that the average correlation coefficient  
16 (R) between the SD from estimation and the ground-measurement is 0.88. We investigated the effects of  
17 wind speed, vapor pressure (VAP), precipitation and aerosol optical depth (AOD) **and cloud capacity** on  
18 the estimated performance of SD, and the results showed that temperature had the greatest effect on SD  
19 estimation. We also found that both too low AOD, **excessive cloud capacity** and too high wind speed  
20 affected the SD estimation on the average annual scale. This high-resolution SD data can provide  
21 important support for accurate radiation resource assessment in China. The SD dataset is freely accessible  
22 at <https://doi.org/10.57760/sciencedb.10276> (Zhang et al., 2024).

## 23 24 1. Introduction

25 Solar radiation is a major driver of photosynthesis and evapotranspiration, plays an indispensable  
26 role in regulating temperature and supporting agricultural production, and has effects on photovoltaic  
27 power generation, making it critical to the Earth's ecosystem and to productive human life (Yu et al.,  
28 2022; Feng et al., 2021). **Satellite remote sensing is an effective method of monitoring and tracking solar  
29 radiation, especially geostationary satellite, which can monitor solar radiation levels in the same target**

**Deleted:** The solar radiation measured by radiation  
observatory can accurately predict solar radiation potential  
and participate in climate change and agricultural production  
model. Nonetheless, the existing radiation data in China is not  
validated through terrestrial observations due to the limited  
number of less than 200 stations in mainland China

36 area several times a day. However, solar radiation inverted by satellite sensors based on reflectance  
 37 information from the land surface is highly susceptible to atmospheric inverted radiation from clouds  
 38 and aerosols, which need to be corrected for by ground measurement radiation stations.  
 39 Unfortunately, there is limited number of radiation observation stations in China (less than 200  
 40 stations in mainland China) and other parts of the world, (Liang et al., 2006; Zhang et al., 2015) for the  
 41 expensive upkeep of terrestrial radiation measured devices, (Zhang et al., 2017; Chukwujindu et al., 2017),  
 42 as well as the lack of widely used empirical physical models for satellite-ground radiation correction,  
 43 making precise tracking of high spatiotemporal solar radiation over time difficult. Sunshine duration (SD)  
 44 is a readily available and cost-effective indicator for monitoring the global radiation resources, and the  
 45 variability of which is determined by a combination of regional factors as well as the solar constant,  
 46 cloud cover, water vapor, and atmospheric pollutants. The SD measured from regular meteorological  
 47 observation has the advantages of long period, good continuity, high spatial density (more than 2000  
 48 stations in mainland China) and reliability, which is considered the best alternative to solar radiation (Xia,  
 49 2010). SD is a key parameter of solar power potential forecasting (Baumgartner et al., 2018; Liu et al.,  
 50 2022), an example is a new SD conversion method based on predicted temperature and weather type data  
 51 for daily-scale solar radiation prediction proposed by Qin et al. (2023). Climate change assessment and  
 52 agricultural production, also need to consider the impact of changes in SD (Ghanghermeh et al., 2022),  
 53 Marsz et al. (2021) suggests that long-term variations in SD in Central Europe are related to changes in  
 54 the annual frequency of macro-types of circulation in the mid-troposphere as well as changes in the  
 55 surface composition of the thermohaline circulation in the North Atlantic. In addition, some researchers  
 56 have found that changes in SD also affect the probability of human diseases (Chang et al., 2022; Gu et  
 57 al., 2019), Liu et al. (2023) observed that insufficient SD (<5.3 hours) was associated with increased  
 58 hospitalisation for schizophrenia, whereas sufficient SD reduced the risk of hospitalisation for  
 59 schizophrenia.  
 60 Accurate inversion of SD is an important reference for agricultural production, solar resource  
 61 utilization and global climate change analysis. Studies on SD have mostly been based on limited ground  
 62 stations (Vivar et al., 2014; Fan et al., 2018; Yao et al., 2018), while SD is affected by atmospheric  
 63 conditions, and it is difficult for a single station to represent this over a large area, so there is a great need  
 64 for a high-resolution SD data based on satellite remote sensing for studies on solar radiation. The  
 65 Advanced Himawari Imager (AHI) instrument, carried on board the new generation of geostationary

Moved down [1]: (Liang et al., 2006; Zhang et al., 2015) for the expensive upkeep of terrestrial radiation

Deleted: measuring devices, making precise tracking of high spatiotemporal solar radiation over time difficult

Moved down [2]: (Zhang et al., 2017; Chukwujindu et al., 2017)

Deleted: )

Moved (insertion) [1]

Moved (insertion) [2]

Deleted: ;

Deleted: ..

Deleted: ), climate

Formatted: Font: +Body (等线), 五号

Deleted: in

Deleted: ). The SD measured from conventional meteorological observation has the advantages of long observation time, good continuity, high spatial density and reliability, which is considered the best alternative to solar radiation (Xia, 2010). Accurate inversion of SD is therefore

Deleted: The Ångström-Prescott model (Ångström, 1924) is the dominant and most widely used model based on SD and solar radiation. The quadratic and cubic forms of the Ångström-Prescott model have been improved and applied to different meteorological conditions (Rietveld, 1978; Bahel et al., ...)

Moved down [3]: 1987; Chen et al., 2004; Wu et al., 2007; Liu et al., 2012; Ampratwum et al., 1999; Elagib et al 2000).

Deleted:

Deleted: Currently, geostationary and polar-orbiting satellite data are widely used for high spatiotemporal resolution ground information tracking, and the

94 satellites -Himawari-8 and 9, has been widely used for the estimating radiation indicators different time  
95 scales for their shortwave radiation products (Damiani et al, 2018; Hou et al., 2020; Letu et al., 2020;  
96 Tana et al., 2023). Meanwhile, the Ångström-Prescott model (Ångström, 1924) is the dominant and most  
97 widely used model based on SD and solar radiation, and the quadratic and cubic forms of the which have  
98 been improved and applied to different meteorological conditions (Rietveld, 1978; Bahel et al., 1987;  
99 Chen et al., 2004; Wu et al., 2007; Liu et al., 2012; Ampratwum et al., 1999; Elagib et al 2000). Therefore,  
100 based on the advantages of high spatiotemporal and temporal resolution of AHI and the existing widely  
101 used empirical relationship model between solar radiation and SD, we can use the radiation products of  
102 AHI to validate the SD data from high-density regular meteorological observation stations in China to  
103 estimate the gridded SD data.

104 In this study, we generate a daily SD dataset in China at a spatial resolution of 5-km using Himawari  
105 AHI L3 shortwave radiation data from 2016 to 2023 fitted with Ångström-Prescott model at different  
106 days of year (DOY). We validated and assessed the accuracy of the daily SD data by the ground-measured  
107 SD and other meteorological data (Wind speed, vapor pressure (VAP) and precipitation) at 2380 Chinese  
108 Meteorological Administration (CMA) stations, as well as the aerosol optical depth (AOD) from MODIS.

## 110 2. Data and method

### 111 2.1 Remote sensing data

112 The geostationary meteorological satellites, Himawari, was launched on 7 October 2014 from the  
113 Japan Meteorological Agency (JMA) in Tane Ashima, Japan, with its hypocenter located at 0.0°N and  
114 140.7°E, approximately 35,800 km above the land surface. In comparison with other geostationary  
115 satellites, Himawari AHI exhibits superior temporal and spatial resolution, reflection band sensitivity and  
116 accuracy (Zhang et al., 2016). The AHI from Himawari-8 and 9 has 16 spectral channels covering the  
117 visible to infrared range, with wavelengths ranging from 0.47 μm to 13.3 μm, providing a wealth of  
118 spectral information (Bessho et al., 2016; Kim et al., 2018; Yu et al., 2019). The temporal and spatial  
119 resolution of the land surface products provided by Himawari AHI is 10 minutes and 5 km respectively,  
120 which is important for understanding the spatiotemporal variations on short time scales (Sawada et al.,  
121 2019).

122 In this study, the Himawari AHI level 3 hourly shortwave radiation (5 km resolution) data from 1  
123 January 2016 to 31 December 2023 was used for SD dataset construction, which calculated by plane-

Deleted: However, there are always biases in

Deleted: AHI radiation data

Deleted: those inverted radiation indicators due to less ground measured stations for validation

Deleted: the susceptibility of remote sensing data to cloud

Deleted: aerosols, while SD reflects both solar radiation and cloud

Moved (insertion) [3]

Deleted: and thus is well suited for inversion using remote sensing radiation data, we can take advantage

Deleted: the

Deleted: SD.

Deleted: 2015

136 parallel theory and considered the top of atmosphere (TOA) radiation by difference between the 300-  
137 3000 nm solar shortwave band and reflected solar radiation by the atmosphere/land surface (Frouin et  
138 al., 2007). This approach assumes that the effects of clouds and clear atmosphere can be decoupled,  
139 which proved to be effective (Dedieu et al., 1987; Frouin and Rachel, 1995). In the event of a one-hour  
140 interval being absent from the imagery, linear interpolation is conducted on each pixel of the missing  
141 imagery based on the time series. In instances where the imagery is absent for a period exceeding one  
142 hour, the day in question is excluded. We calculate the daily average shortwave radiation in China based  
143 on China Standard Time (CST) using this hourly AHI shortwave radiation data.

144 The MCD19A2 is a MODIS Terra and Aqua combined multi-angle Implementation of Atmospheric  
145 Correction (MAIAC) Land AOD gridded Level 2 product produced daily at 1 km pixel resolution, which  
146 corrected for atmospheric gases and aerosols using a new MAIAC algorithm that is based on a time series  
147 analysis and a combination of pixel- and image-based processing (Lyapustin et al., 2022). In this study,  
148 the AOD at 550 nm in MCD19A2 from 2016 to 2023 were collected using Google Earth Engine (GEE)  
149 (Gorelick et al., 2017).

## 150 2.2 Ground Measurements data

151 The ground measurements in CMA from 1 January 2016 to 31 December 2023 used to perform SD  
152 estimation. The spatial coverage of Himawari covers 2380 CMA automatic meteorological stations in  
153 China. The CMA performs quality control of the data, including spatiotemporal consistency checks and  
154 manual corrections and adjustments before releasing the meteorological data (Moradi, 2009; Tang et al.,  
155 2010). Although the quality of the ground-based measurements should have been controlled before  
156 acquisition, there was still a need for a more stringent check on the quality of the data based on the daily  
157 meteorological data reconstruction method from CMA (Zhang et al., 2015). Figure 1 shows the spatial  
158 distribution of 2380 meteorological. In this study, daily SD, vapor pressure (VAP), temperature, wind  
159 speed, cloud capacity and precipitation from the CMA automatic meteorological stations were used to fit  
160 and validate the grid-dataset as well as to analyze the factors influencing the estimated performance,  
161 respectively, and March-May was classified as spring, June-August as summer, September-November as  
162 autumn and December-February as winter.

Deleted: methodology of

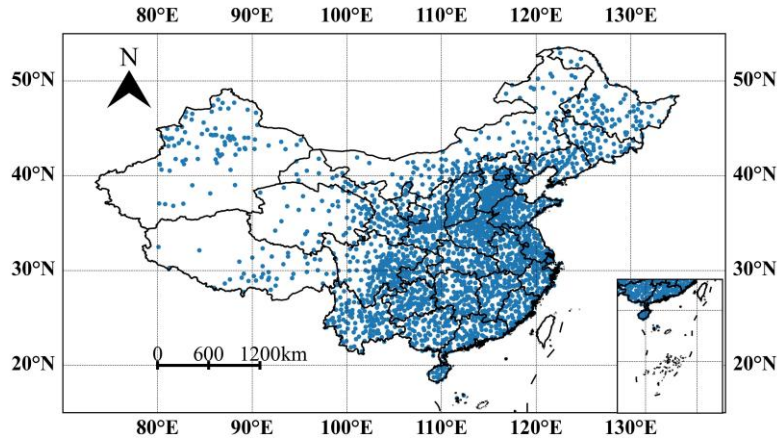


Figure 1. Spatial distribution of the 2380 automatic meteorological stations of the China Meteorological Administration (CMA).

### 2.3 Model overview

The Ångström-Prescott model is an empirical model which based on the relationship between SD and solar radiation, and is widely used in meteorology and agricultural science. The model was proposed by Ångström based on total solar radiation on clear days and improved by Prescott on the basis of astronomical radiation (Ångström, 1924) with the following equations:

$$R_s = (a + b \frac{n}{N}) R_a \quad (1)$$

where  $R_s$  is the total solar radiation reaching the surface,  $R_a$  is the astronomical radiation,  $a$  and  $b$  are empirical coefficients,  $n$  is the actual SD, and  $N$  is the maximum SD available.  $R_a$  and  $N$  counts are calculated with reference to Liu et al. (2009):

$$R_a = 37.6 d_r (\omega_s \sin \phi \sin \delta + \cos \phi \cos \delta \sin \omega_s) \quad (2)$$

$$d_r = 1 + 0.033 \cos(\frac{2\pi}{365} \text{DOY}) \quad (3)$$

$$\delta = 0.4093 \sin(\frac{2\pi}{365} \text{DOY} - 1.39) \quad (4)$$

$$\omega_s = \arccos(-\tan\phi \tan\delta) \quad (5)$$

$$N = \frac{24}{\pi} \omega_s \quad (6)$$

176 where  $d_r$  is the eccentricity of the Earth's orbit around the Sun,  $\omega_s$  is the angle at sunset,  $\phi$  is the latitude,  
177  $\delta$  is the inclination angle of the sun, and DOY is the days of a year. We considered Himawari AHI level  
178 3 hourly shortwave radiation as the  $R_s$  in this model, and SD of ground-based observation as a  
179 validation of  $n$ , and the parameters  $a$  and  $b$  of Ångström-Prescott model were fitted using the least-squares  
180 method.

#### 181 2.4 Validation

182 We divided the original data into a training set (more than  $5 \times 10^6$  grid cells during 2017-2022) and  
183 a testing set (2016 and 2023, [for there is a widespread transition from manual to automatic SD recorders](#)  
184 [in 2019 or station relocations \(He et al., 2024\)](#)). In order to identify the best Ångström-Prescott model  
185 and its corresponding parameters, the performance of the Ångström-Prescott model on the training set  
186 (2017-2022) was evaluated using a 100-fold cross-validation (CV) approach, using a DOY-based CV  
187 strategy. In each iteration of each DOY, 99 folds were used as the training set and the remaining folds as  
188 the validation set, and the training and validation process was repeated 100 times to obtain the best model  
189 parameters  $a$  and  $b$  for each DOY. In addition, the 2016 and 2023 ground-based SD data were used as  
190 the test data to evaluate the generalization capability of the best model parameters  $a$  and  $b$  at each DOY.  
191 The specific process is shown in Figure 2. Pearson correlation coefficient (R) and root mean square error  
192 (RMSE) were calculated to evaluate the performance of the model.

Deleted: ).

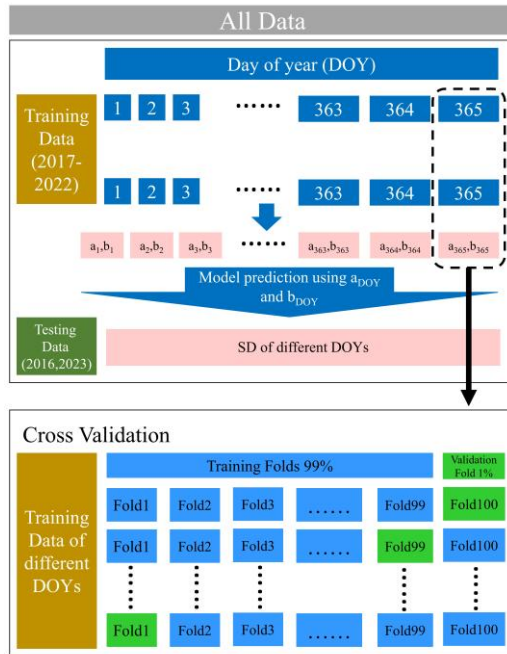


Figure2. Detailed process of model cross-validation and testing.

194

195

196 **2.5 Methods of spatiotemporal variation analysis**

197 Empirical orthogonal function (EOF) decomposition is a significant technique used to investigate  
 198 the geographical and temporal fluctuations in meteorological characteristics (Zhou et al., 2021). The  
 199 variable field can be decomposed into two parts: a spatial function that remains constant across time and  
 200 a temporal function that changes exclusively with time, thus the primary spatial and temporal variations  
 201 of which are evident in the area with a significant contribution to the variance. The spatial function  
 202 component comprises several mutually independent and orthogonal spatial modes, also considered as  
 203 eigenvectors. The temporal function part consists of the projection of the spatial modes in time, which is  
 204 represented by the time coefficients. We used EOF to analyze spatiotemporal variations of the established  
 205 SD dataset in China, then the original variable field information and spatial coefficients is concentrated  
 206 in the first few modes.

207

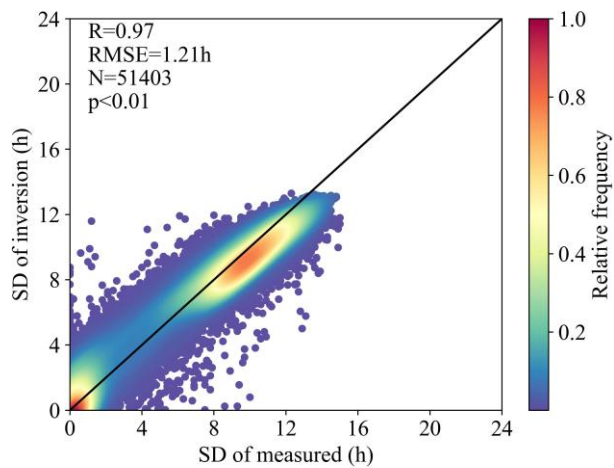
208 **3. Results**

209 **3.1 Evaluation of the training data**

210 Figure 3 shows the estimation results of the CV sampling method for all DOYs in the training set  
211 (N=68806), an R value of 0.9695 was obtained for the entire training set, with a corresponding RMSE  
212 value of 1.2h. The measured and inverted SD converge to the 1:1 trend line, but overestimation occurs  
213 in the dense region around 10h. Figure 4 discusses the inverse performance of the different seasons in  
214 the training set separately. The SD is significantly higher in spring and summer than in autumn and winter,  
215 which is more concentrated in the 0h and 10h regions in winter. From Figure 4 it can be seen that in  
216 spring the highest R value is 0.9747 and RMSE value is 1.18h, while in winter the lowest RMSE value  
217 is 1.13h. However, in summer the highest RMSE value is 1.3h, and it is obvious that the estimation in  
218 summer performs the worst when the measured SD is 0h. The measured and inverted SD in spring most  
219 converge to the 1:1 trendline, while overestimation of which occurs in the dense region around 10h in  
220 winter.

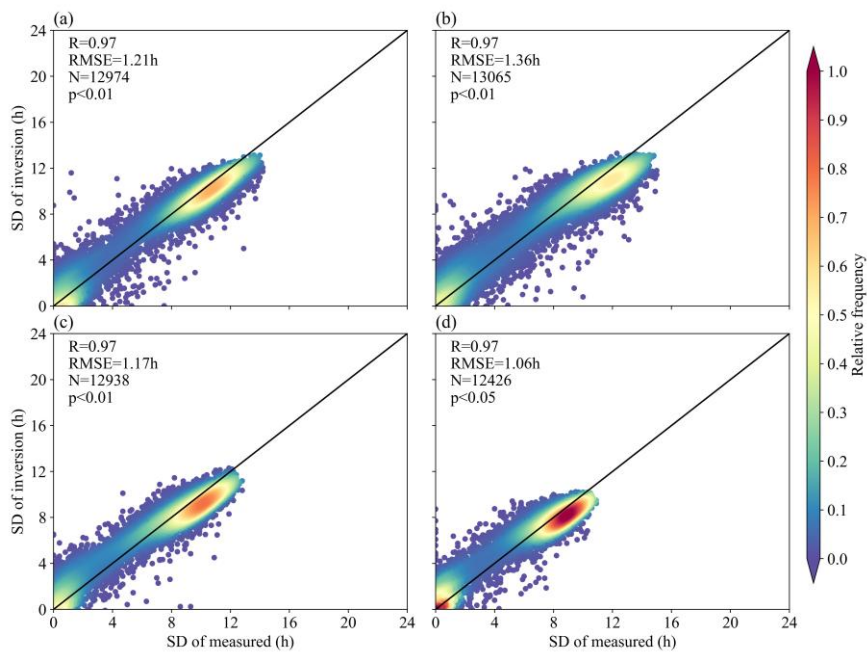
221 Figure 5 shows the optimal Ångström-Prescott model parameters a and b at different DOYs. The  
222 parameter a has an upward parabolic trend with DOY, with a local maximum value of 0.22 at DOY =  
223 306 and a local minimum value of 0.13 at DOY = 351. Parameter b showed a significant "W"-shaped  
224 variation with DOY, with a local maximum value of 0.74 at DOY = 146 and two local minimum values  
225 of 0.66 and 0.63 at DOY = 99 and 351. In general, parameters a and b of Ångström-Prescott model are  
226 characterized by more pronounced seasonal variations. Figure 6 shows the variation of the training set  
227 evaluation indicator (R and RMSE) with DOY. More than half of the DOYs had R values greater than  
228 the overall R value in Figure 3, but there were still 134 days with R values less than 0.97 and a minimum  
229 value of 0.94 at DOY = 193. Meanwhile more than half of the DOYs have RMSE values less than the  
230 overall RMSE values in Figure 3, but there are still 157 days with R values less than 1.2h, and again  
231 there is a maximum value of 2.1h for RMSE at DOY = 193. The evaluation indicator for the training set  
232 were not characterized by significant seasonal variations.





233  
234  
235

Figure 3. Estimation results of the CV sampling method in training set



236  
237  
238

Figure 4. Estimation results of the CV sampling method in training set from different seasons ((a) spring, (b) summer, (c) autumn, (d) winter).

239

240

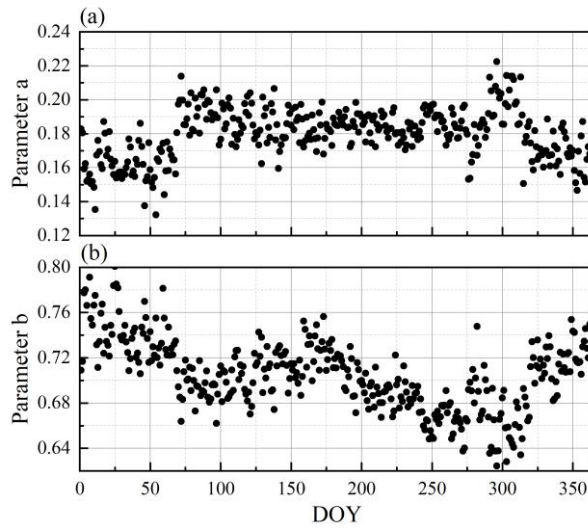


Figure 5. The a and b coefficients of Ångström-Prescott model for different DOYs.

241

242 Figure 6. The correlation coefficients (R) (a) and RMSE (b) of CV sampling method in training set for

243

different DOYs.

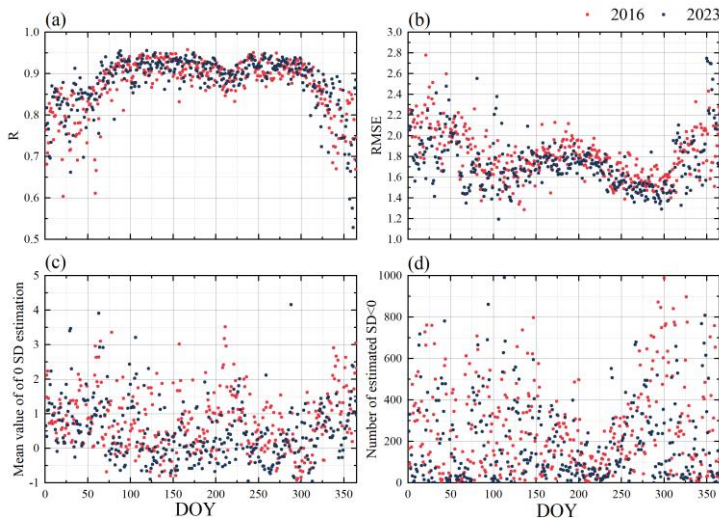
244

### 245 3.2 Evaluation of the testing data

246 The different evaluation indicator for the test set (2016 and 2023) are given in Figure 7, respectively.

247 Figure 7(a) shows the R of 2016 and 2023, with the trends in these two years are essentially the identical,

248 with an "M" shape. The average R value for 2016 is 0.88, which is generally consistent with 2023. The  
 249 minimum R value of 0.52 in 2023 (DOY=361) was lower than that of 0.60 in 2016 (DOY=21), but both  
 250 occurred in winter. The trend of RMSE values for 2016 and 2023 is opposite to the R value, with the  
 251 maximum and minimum RMSE values occurring in 2023 at 2.77 (DOY=355) and 1.19 (DOY=106),  
 252 respectively. Figures 7(c) and (d) show the estimated performance of the 0 SD (no sunshine for the whole  
 253 day) for the CMA meteorological stations in 2016 and 2023. Figure 7(c) shows the estimated mean values  
 254 of 0 SD for different DOYs in 2016 and 2023, where the mean value in 2023 (0.49h) is smaller than in  
 255 2016 (0.75h), with the maximum and minimum mean values still occurring in 2023 at 3.42 (DOY=211)  
 256 and -0.75 (DOY=134), respectively. Figure 7(d) gives the number of estimated SD less than 0 for  
 257 different DOYs in 2016 and 2023, of which there were more average daily estimated SDs less than 0 in  
 258 2016 than in 2023, at 267/day, with the lowest value also occurring in 2016, at 997 for DOY=294. The  
 259 bias in the 0SD estimation is linked to the over- and under-representation of its number. Changing all  
 260 estimated SD less than 0 to 0 resulted in an improvement in their estimated performance (Figure 8), with  
 261 2016 having a greater improvement than 2023 and having the greatest improvement with DOY=285.  
 262



263

264

Figure 7. Estimated performance in testing set.

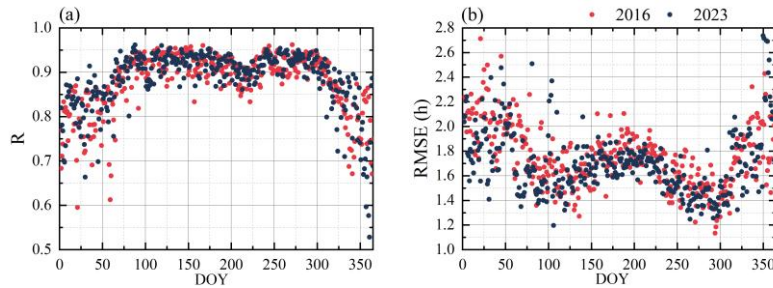


Figure 8. Estimated performance by changing all estimated SD less than 0 to 0 in testing set.

### 3.3 Effect of different environmental factors on SD estimation

Figure 9 shows the effect of national daily average VAP, precipitation, and temperature (based on CMA meteorological stations) on R values in Figure 8. The R values is exponentially related to both VAP and precipitation, and VAP has a greater effect on R than precipitation. Meanwhile the estimated performance in 2016 is more affected by moisture conditions. Temperature has the greatest impact on R, with 2023 being affected to a greater extent than 2016 (Figure 9 (e, f)). The influences on SD estimation are discussed by distinguishing the different seasons (Table 1), with VAP, precipitation and temperature having the greatest influence on R values in autumn and the least in winter. It is worth noting that R in summer were negatively correlated with VAP and temperature.

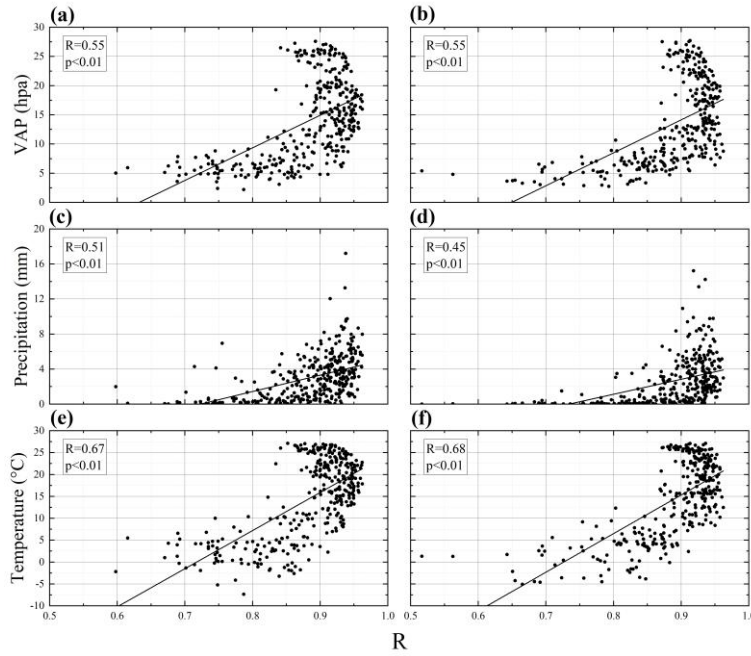
Figure 10 and 11 shows the annual average SD from CMA meteorological station and Himawari estimation in 2016 and 2023 respectively, along with the annual average AOD, wind speed, and cloud capacity. On annual scale, ground-measured and estimated SD are in better consistency in eastern and northern China, while both years have higher estimates in eastern China and lower estimates in northwestern and northeastern China, comparing the impact factors, higher wind speed and lower AOD in these areas both affected the SD estimation. The estimated SD appears to be overestimated (southern China) at excessively high cloud cover, especially at excessively high low cloud cover, which is more pronounced in 2016, while in 2023 the total cloud cover is higher, the low-cloud cover is lower, and the estimation error has poorer feedback on the cloud cover.

Deleted: and

Deleted: .

Deleted: an

Deleted: site



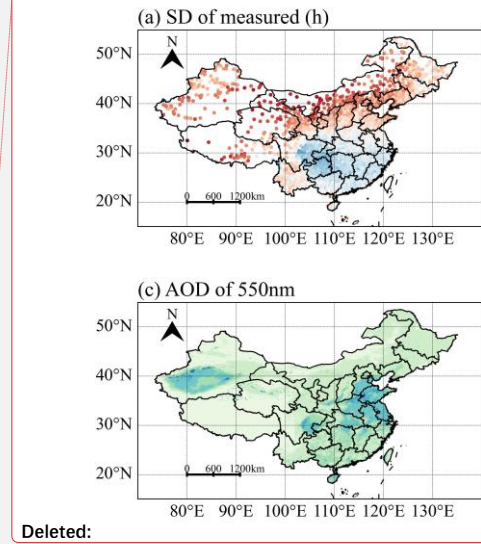
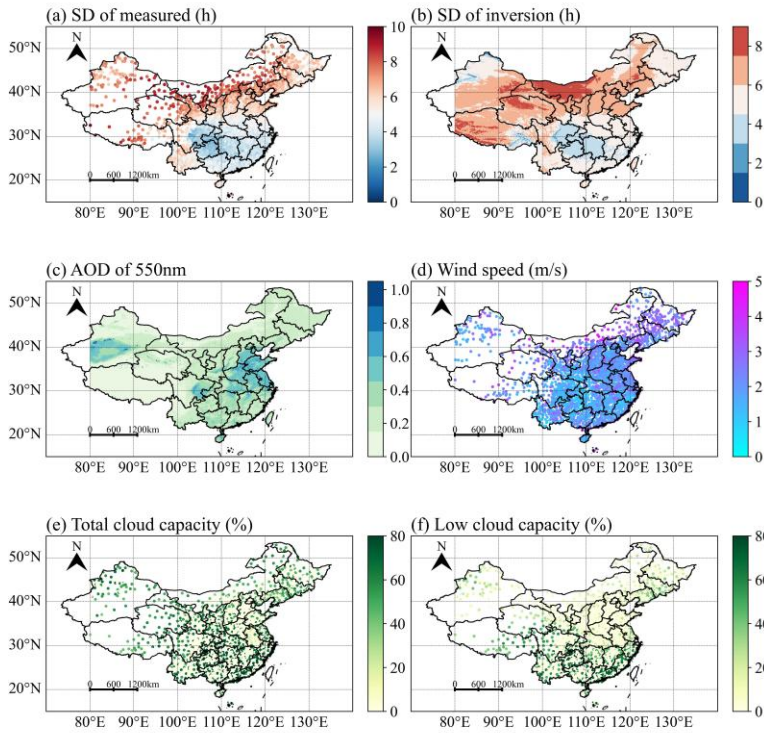
290  
 291 Figure 9. R values and different environmental factors (VAP (a, b), Precipitation (c, d), Temperature (e,  
 292 f)) correlations in 2016 (a, c and e) and 2023 (b, d and f).

293

294 **Table 1.** Correlation coefficients between estimated performance and influencing factors in different  
 295 seasons (\* and \*\* refer to passing the  $p < 0.05$  and  $p < 0.01$  significance tests, respectively)

Time	Influencing Factors		
	VAP	Precipitation	Temperature
Spring	0.29*	0.43**	0.31*
Summer	-0.56*	0.28*	-0.53**
Autumn	0.59**	0.46**	0.62**
Winter	0.28*	0.26**	0.22**

296



297

298

299

300

Figure 10. Comparison of annual average ground measurement (a) and Himawari (b) SD in 2016, giving annual average AOD of 550nm (c), the wind speed (d) total cloud capacity (e) and low cloud capacity (f).

Deleted: ) and



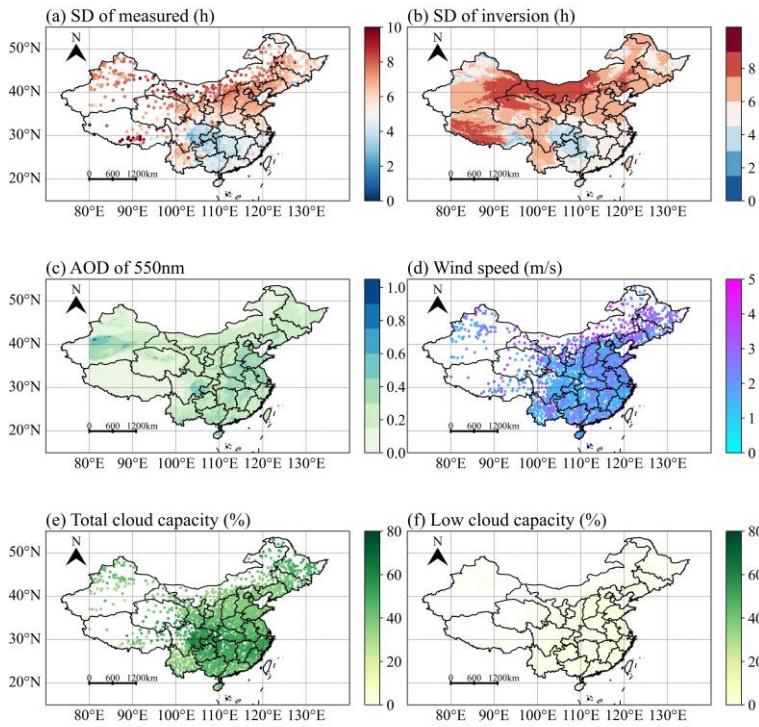
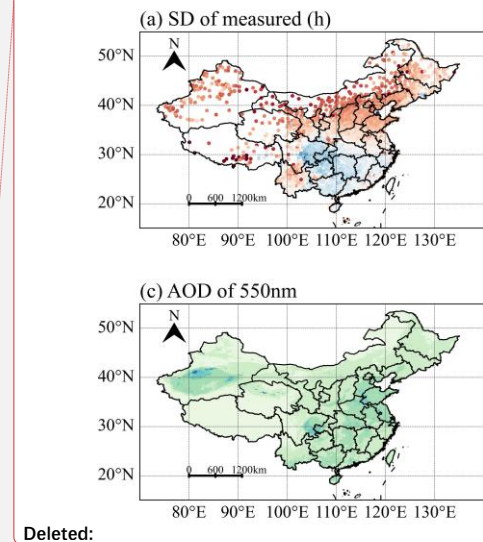


Figure 11. Same as Figure 10, but in 2023.



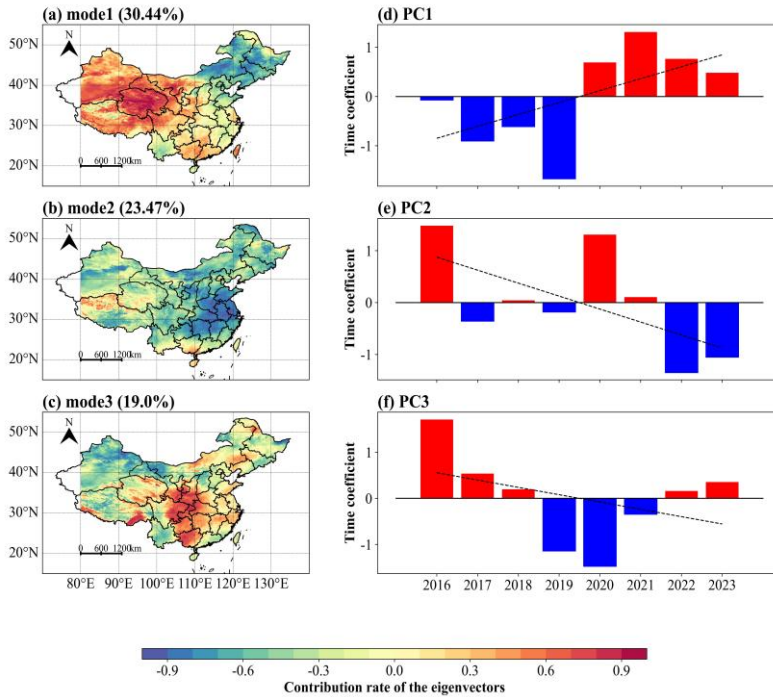
Deleted:

Deleted: 3

### 3.4 Effect of different environmental factors on SD estimation

EOF analysis of mean annual SD grid-data in China from 2015-2023, the spatial variance contribution rate of the eigenvectors in the first three EOF modes are shown in Figure 12, where the explained variance of each mode is 30.44%, 23.47% and 19.0%, respectively, with a cumulative variance contribution of about 72.91%. The variance contribution rate of mode 1 eigenvectors in Figure 12a surpasses that of other models, making it the predominant spatial distribution in China. The mode 1 decreases from western to eastern China, the northwest China exhibits extremely low values, but there are exceptions in Yunnan Province. The mode 2 (Figure 12b) exhibits a dipolar-type of distribution decreasing from the southern to northeast China, and the mode 3 shows a tri-pole distribution decreasing from central China to sides. Generally, it can be concluded that the SD decreases from western to northern China. Figure 12def shows the time coefficients of SD from the first three models in China, the SD time coefficients of the mode 1 (Figure 12d) shows an increasing trend from 2016 to 2023, with the minimum

320 time coefficient in 2019 and maximum time coefficient in 2021. It can be seen from Figure 12ef that the  
 321 SD time coefficients of the mode 2 and 3 show a decreasing trend, and both are positive in 2016 and  
 322 negative in 2019.



323  
 324 Figures 12. Distribution of eigenvectors contribution rate (a-c) and time coefficients (d-f) for the first  
 325 three modes of SD.  
 326

327 **4. Discussion**

328 There is no explicit remote sensing inversion model for SD as its observation is founded upon the  
 329 accumulation of radiation. Consequently, SD datasets were constructed through the spatial interpolation,  
 330 which results in the absence of SD datasets that are released with high spatiotemporal resolution. In this  
 331 study, a 5km-resolution SD dataset in China from 2016 to 2023 has been established based on time series  
 332 using Himawari imagery fitted with Ångström-Prescott model, which previous studies have not been  
 333 conducted.

334 The time series based Ångström-Prescott model was used to invert the SD in China, setting the



335 coefficients of a and b to fixed values for the whole region at different DOYs, while the suggested  
336 coefficients in this study are not comparable with the calibrated coefficients for other regions. Previous  
337 studies on the Ångström-Prescott model have confirmed that it is a reliable tool for estimating solar  
338 energy in practical applications, with no significant dependence of its accuracy on latitude (Paulescu et  
339 al., 2016). It has also been confirmed that the model's accuracy has a strong dependence on and season  
340 (Liu et al., 2023) according to the results of the present study (Figure 4-8), the cause of which can be  
341 attributed to differences in the length of day and night in different seasons. This work not only forms a  
342 more accurate evaluation standard for the level of radiation received on the ground, but also provides a  
343 better support for the radiation estimation in the future, and more conventional meteorological stations  
344 will be established in the future to validate and improve the Ångström-Prescott model based on time-  
345 series. A fact that cannot be ignored is that the number of meteorological observation stations in  
346 southwestern China (especially in the Tibetan Plateau Region) is small and spatially distributed unevenly,  
347 and the snow in the plateau seriously affects the judgement of the reflectance data from the Himawari  
348 imagery, and we will consider the input of the land cover characteristics as the climatological data in the  
349 following to improve this poor performance.

350 It is worth noting that there is a bias in the validation of the training and test data, where there is an  
351 overestimation at OSD (Figure 3), may be the strong light in almost most of the area under a DOY leads  
352 to Ångström-Prescott model larger parameters and over-estimation of a very small portion of the image  
353 elements that contain aerosols, clouds and even precipitation. In addition, it also occurred in the test data  
354 that the estimated SD was less than 0 (Figure 7 cd), because the thicker clouds, atmospheric aerosols and  
355 water vapor in majority of the area on that day did not have much effect on the ground-based SD  
356 instrument (the atmospheric longwave radiation contained in the direct radiation was not affected), but  
357 had a significant effect on the AHI shortwave radiation data, resulting in SD less than 0. After changing  
358 the image elements with SD less than 0 to 0, the validation results are still substantial (Figure 8),  
359 indicating that this part of radiation is essentially less than the threshold for SD observations ( $120 \text{ W/m}^2$ ).  
360 In conclusion, as our approach is carried out based on time series, it is unavoidable that we will encounter  
361 input data that are not sensitive to different sky conditions. In the future, the use of relevant physical  
362 precipitation models will be considered to simulate the precipitation process at different times of the day  
363 based on the radiation data. This will enable us to estimate SD, and this aspect of the Ångström-Prescott  
364 model will be improved subsequently.

365 We found that temperature, moisture conditions, wind speed and atmospheric pollutants all  
366 influence the SD estimation, with temperature having the greatest effect in temporal variation and wind  
367 speed having a stronger effect in spatial variation compared with AOD, and cloud capacity. However, we  
368 believe that the effects of these environmental factors are not independent, but are the result of interaction  
369 (Tang et al., 2022). In densely populated and economically developed areas (eastern and southern China),  
370 where pollutant levels are higher and increased wind speed accelerates their dispersion, this regulatory  
371 mechanism is enhanced with increasing pollutants (O'Dowd et al., 1993; Wang et al., 2014). An increase  
372 or decrease in wind speed affects the rate of diffusion of water vapor and pollutants in the air, which in  
373 turn affects atmospheric transparency and ultimately the SD estimation. However, the effect of  
374 temperature on SD estimation in this study are not consistent with some previous studies (Tang et al.,  
375 2022; Feng et al., 2019; Ren et al., 2017), which suggests that the relationship between SD and  
376 temperature and relative humidity is complex and needs to be further determined in future studies.

377 The EOF method analysis of mean annual SD declare that it decreases from western to northeast  
378 China, which is consistent with the Tang et al. (2022) and Xiong et al. (2020), suggesting that the pattern  
379 of industrial development between western to eastern China is affecting radiation levels to some extent.  
380 The time coefficients of EOF show that there is a certain degree of increase in SD in recent years, which  
381 is closed to long-term SD analysis from Tang et al. (2022). This trend may be related to global climate  
382 change (Josefsson and Landelius, 2000), because of the variation in wind speeds due to global warming  
383 has resulted in decreased cloud dissipation across mainland China (Xiong et al., 2020). In addition, the  
384 decrease in human activities in recent years (Liu et al., 2020) has also contributed to a weakening of the  
385 urban rain island effect and aerosols (Glantz et al., 2006), and it appears that the latter factor is more  
386 influential from this study. However short-term reductions in human activity cannot become the norm,  
387 and sunshine duration are bound to fluctuating changes due to the acceleration of the hydrological cycle.

388

#### 389 5. Data availability

390 The SD dataset is freely accessible at <https://doi.org/10.57760/sciencedb.10276> (Zhang et al., 2024).

#### 391 6. Conclusion

392 We have introduced a newly developed high-resolution dataset, which provides SD in China for the  
393 period 2016–2023. We calculated daily SD by Himawari Level 3 shortwave radiation fitted with the  
394 Ångström-Prescott model based on time series, and used ground-measured SD to evaluate the estimation

Deleted: .

396 performance. The validation of testing data from ground-measured SD gave favorable results, with R  
397 values greater than 0.5 and an average of 0.88 for all days in 2016 and 2023. We also found that  
398 temperature and wind speed dominate the Ångström-Prescott model estimating SD. A future direction  
399 for this study would be to divide the Chinese regions into suitable areas to independently estimate and  
400 synthesize a more accurate daily SD dataset in China.

401

402 **Author contributions.** ZZ and SF designed and organized the paper. ZZ and JH prepared the related  
403 materials and ran the dataset. ZZ evaluated the accuracy of the dataset. All authors discussed the results  
404 and commented on the paper.

405

406 **Competing interests.** The contact author has declared that none of the authors has any competing  
407 interests.

408

409 **Financial support.** This research was supported by the National Key Research and Development  
410 Program of China (grant no. 2023YFE0122200), the National Nature Sciences Foundation (grant no.  
411 42075193).

412

#### 413 Reference

414 Ampratwum, D. B. and Dorvlo, A. S.: Estimation of solar radiation from the number of sunshine hours.  
415 Appl. Energy, 63(3), 161-167. [https://doi.org/10.1016/S0306-2619\(99\)00025-2](https://doi.org/10.1016/S0306-2619(99)00025-2), 1999.

416 Ångström A.: Solar and terrestrial radiation. Report to the international commission for solar research on  
417 actinometric investigations of sola and atmospheric radiation. Q J Roy Meteor Soc., 50:121–6.  
418 <https://doi.org/10.1002/qj.49705021008>, 1924.

419 Bahel, V., Bakhsh, H. and Srinivasan, R.: A correlation for estimation of global solar radiation. Energy,  
420 12, 131-135. [https://doi.org/10.1016/0360-5442\(87\)90117-4](https://doi.org/10.1016/0360-5442(87)90117-4), 1987.

421 [Baumgartner, D., Pötzi, W., Freislich, H., Strutzmann, H., Veronig, A.M., Foelsche, U. and Rieder, H.E.  
422 A comparison of long-term parallel measurements of sunshine duration obtained with a Campbell-Stokes  
423 sunshine recorder and two automated sunshine sensors. Theor. Appl. Climatol., 133, 263-275.  
424 <https://doi.org/10.1007/s00704-017-2159-9>, 2018.](https://doi.org/10.1007/s00704-017-2159-9)

425 Bessho, K., Date, K., Hayashi, M., Ikeda, A., Imai, T., Inoue, H., Kumagai, Y., Miyakawa, T., Murata,  
426 H., Ohno, T., Okuyama, A., Oyama, R., Sasaki, Y., Shimazu, Y., Shimoji, K., Sumida, Y., Suzuki, M.,  
427 Taniguchi, H., Tsuchiyama, H., Uesawa, D., Yokota, H. and Yoshida, R.: An introduction to Himawari-  
428 8/9—Japan's new-generation geostationary meteorological satellites. J. Meteorol. Soc. Japan., Ser. II,  
429 94(2), 151-183. <https://doi.org/10.2151/JMSJ.2016-009>, 2016.

430 Chang, Z., Chen, Y., Zhao, Y., Fu, J., Liu, Y., Tang, S., Han, Y. and Fan, Z.: Association of sunshine  
431 duration with acute myocardial infarction hospital admissions in Beijing, China: A time-series analysis  
432 within-summer. The Science of the total environment, 154528.  
433 <https://doi.org/10.1016/j.scitotenv.2022.154528>, 2022.

434 Chen, R., Ersi, K., Yang, J., Lu, S. and Zhao, W.: Validation of five global radiation models with measured

**Deleted:** Ångström A.: Solar and terrestrial radiation. Report to the international commission for solar research on actinometric investigations of sola and atmospheric radiation. Q J Roy Meteor Soc., 50:121–6. <https://doi.org/10.1002/qj.49705021008>, 1924.

440 daily data in China. *Energy Convers. Manage.*, 45, 1759-1769.  
441 <https://doi.org/10.1016/J.ENCONMAN.2003.09.019>, 2004.

442 Chukwujindu, N.S.: A comprehensive review of empirical models for estimating global solar radiation  
443 in Africa. *Renew. Sust. Energ. Rev.*, 78, 955-995. <https://doi.org/10.1016/J.RSER.2017.04.101>, 2017.

444 Damiani, A., Irie, H., Horio, T., Takamura, T., Khatri, P., Takenaka, H., Nagao, T.M., Nakajima, T.Y.: and  
445 Cordero, R.R. Evaluation of Himawari-8 surface downwelling solar radiation by SKYNET observations.  
446 *Atmos. Meas. Tech. Discuss.*, 1-28. <https://doi.org/10.5194/AMT-2017-440>, 2018.

447 Dedieu, G., P. Y. Deschamps, and Y. H. Kerr.: Satellite estimation of solar irradiance at the surface of the  
448 earth and of surface albedo using a physical model applied to Metcosat Data. *J. Appl. Meteorol. Climatol.*,  
449 26.1: 79-87. [https://doi.org/10.1175/1520-0450\(1987\)026<0079:SEOSIA>2.0.CO;2](https://doi.org/10.1175/1520-0450(1987)026<0079:SEOSIA>2.0.CO;2), 1987.

450 Elagib, N.A. and Mansell, M.G.: New approaches for estimating global solar radiation across Sudan.  
451 *Energy Convers. Manage.*, 41, 419-434. [https://doi.org/10.1016/S0196-8904\(99\)00123-5](https://doi.org/10.1016/S0196-8904(99)00123-5), 2000.

452 Fan, J., Wang, X., Wu, L., Zhang, F., Bai, H., Lu, X. and Xiang, Y.: New combined models for estimating  
453 daily global solar radiation based on sunshine duration in humid regions: A case study in South China.  
454 *Energy Convers. Manage.*, 156, 618-625. <https://doi.org/10.1016/J.ENCONMAN.2017.11.085>, 2018.

455 Feng, Y., Zhang, X., Jia, Y., Cui, N., Hao, W., Li, H. and Gong, D.: High-resolution assessment of solar  
456 radiation and energy potential in China. *Energy Convers. Manage.*, 240, 114265.  
457 <https://doi.org/10.1016/j.atmosenv.2022.119286>, 2021.

458 Feng, Z., Guo, B., Ren, S. and Li, Y.: Reduction in sunshine duration and related factors over mainland  
459 China during 1961–2016. *Energies*, 12(24), 4718. <https://doi.org/10.3390/en12244718>, 2019.

460 Frouin, R. and Murakami, H.: Estimating photosynthetically available radiation at the ocean surface from  
461 ADEOS-II global imager data. *J. Oceanogr.*, 63, 493-503. <https://doi.org/10.1007/S10872-007-0044-3>,  
462 2007.

463 Frouin, Robert, and Rachel T. Pinker.: Estimating photosynthetically active radiation (PAR) at the earth's  
464 surface from satellite observations. *Remote Sens Environ.*, 51.1: 98-107. [https://doi.org/10.1016/0034-4257\(94\)00068-X](https://doi.org/10.1016/0034-4257(94)00068-X), 1995.

466 Ghanghermeh, A., Roshan, G. and Halabian, A.: Projecting spatiotemporal variations of sunshine  
467 duration with regards to climate change in Iran as a step towards clean energy. *Sustain. Energy Technol.*  
468 *Assess.*, 53, 102630. <https://doi.org/10.1016/j.seta.2022.102630>, 2022.

469 Glantz, P., Nilsson, D.E. and Hoyningen-Huene, W.V. Estimating a relationship between aerosol optical  
470 thickness and surface wind speed over the ocean. *Atmos. Chem. Phys.*, 6, 11621-11651.  
471 <https://doi.org/10.5194/ACPD-6-11621-2006>, 2006.

472 Gorelick, N., Hancher, M., Dixon, M., Ilyushchenko, S., Thau, D. and Moore, R.: Google Earth Engine:  
473 Planetary-scale geospatial analysis for everyone. *Remote Sens Environ.*, 202, 18-27.  
474 <https://doi.org/10.1016/J.RSE.2017.06.031>, 2017.

475 Gu, S., Huang, R., Yang, J., Sun, S., Xu, Y., Zhang, R., Wang, Y., Lu, B., He, T., Wang, A., Bian, G. and  
476 Wang, Q.: Exposure-lag-response association between sunlight and schizophrenia in Ningbo, China.  
477 *Environ. Pollut.*, 247, 285-292. <https://doi.org/10.1016/j.envpol.2018.12.023>, 2019.

478 [He, Y., Wang, K., Yang, K., Zhou, C., Shao, C., and Yin, C.: Homogenized daily sunshine duration over](https://doi.org/10.5194/essd-2024-493)  
479 [China from 1961 to 2022. \*Earth Syst. Sci. Data Discuss.\* \[preprint\], \[https://doi.org/10.5194/essd-2024-\]\(https://doi.org/10.5194/essd-2024-493\)](https://doi.org/10.5194/essd-2024-493)  
480 [493, in review, 2024.](https://doi.org/10.5194/essd-2024-493)

481 Hou, N., Zhang, X., Zhang, W., Wei, Y., Jia, K., Yao, Y., Jiang, B. and Cheng, J.: Estimation of Surface  
482 Downward Shortwave Radiation over China from Himawari-8 AHI Data Based on Random Forest.  
483 *Remote. Sens.*, 12, 181. <https://doi.org/10.3390/rs12010181>, 2023.

484 Josefsson, W. and Landelius, T. Effect of clouds on UV irradiance: As estimated from cloud amount,  
485 cloud type, precipitation, global radiation and sunshine duration. *J. Geophys.*, 105, 4927-4935.  
486 <https://doi.org/10.1029/1999JD900255>, 2000.

487 Kim, B., Lee, K., Jee, J. and Zo, I.: Retrieval of outgoing longwave radiation at top-of-atmosphere using  
488 Himawari-8 AHI data. *Remote Sens Environ.*, 204, 498-508. <https://doi.org/10.1016/J.RSE.2017.10.006>,  
489 2018.

490 Letu, H., Yang, K., Nakajima, T.Y., Ishimoto, H., Nagao, T.M., Riedi, J.C., Baran, A.J., Ma, R., Wang,  
491 T., Shang, H., Khatri, P., Chen, L., Shi, C. and Shi, J.: High-resolution retrieval of cloud microphysical  
492 properties and surface solar radiation using Himawari-8/AHI next-generation geostationary satellite.  
493 *Remote Sens Environ.*, 239, 111583. <https://doi.org/10.1016/j.rse.2019.111583>, 2020.

494 Liang, S., Zheng, T., Liu, R., Fang, H., Tsay, S. and Running, S.W.: Estimation of incident  
495 photosynthetically active radiation from Moderate Resolution Imaging Spectrometer data. *J. Geophys.*  
496 *Res.*, 111. <https://doi.org/10.1029/2005JD006730>, 2006.

497 Liu, F., Wang, X., Sun, F. and Wang, H.: Correct and remap solar radiation and photovoltaic power in  
498 China based on machine learning models. *Appl. Energy*, 312, 118775.  
499 <https://doi.org/10.1016/j.apenergy.2022.118775>, 2022.

500 Liu, J., Liu, J., Linderholm, H.W., Chen, D.L., Yu, Q., Wu, D. and Haginoya, S.: Observation and  
501 calculation of the solar radiation on the Tibetan Plateau. *Energy Convers. Manage.*, 57, 23-32.  
502 <https://doi.org/10.1016/J.ENCONMAN.2011.12.007>, 2012.

503 Liu, J., Shen, Y., Zhou, G., Liu, D., Yu, Q. and Du, J.: Calibrating the Ångström–Prescott Model with  
504 Solar Radiation Data Collected over Long and Short Periods of Time over the Tibetan Plateau. *Energies*.  
505 <https://doi.org/10.3390/en16207093>, 2023.

506 Liu, L., Wu, Q., Li, X., Song, R., Wei, N., Liu, J., Yuan, J., Yan, S., Sun, X., Liang, Y., Li, Y., Jin, X., Wu,  
507 Y., Mei, L., Song, J., Yi, W., Pan, R., Cheng, J. and Su, H. [Sunshine duration and risks of schizophrenia  
508 hospitalizations in main urban area: Do built environments modify the association? \*The Sci. Total  
509 Environ.\* 162057. <https://doi.org/10.1016/j.scitotenv.2023.162057>, 2023.](https://doi.org/10.1016/j.scitotenv.2023.162057)

510 Liu, Q., Sha, D., Liu, W., Houser, P.R., Zhang, L., Hou, R., Lan, H., Flynn, C., Lu, M., Hu, T. and Yang,  
511 C. Spatiotemporal Patterns of COVID-19 Impact on Human Activities and Environment in Mainland  
512 China Using Nighttime Light and Air Quality Data. *Remote. Sens.*, 12, 1576.  
513 <https://doi.org/10.3390/rs12101576>, 2020.

514 Liu, X., Mei, X., Li, Y., Wang, Q., Zhang, Y. and Porter, J. R.: Variation in reference crop  
515 evapotranspiration caused by the Ångström–Prescott coefficient: Locally calibrated versus the FAO  
516 recommended. *Agric Water Manag.*, 96(7), 1137-1145. <https://doi.org/10.1016/J.AGWAT.2009.03.005>,  
517 2009.

518 Lyapustin, A. and Wang, Y.: MODIS/Terra+ Aqua Land Aerosol Optical Depth Daily L2G Global 1km  
519 SIN Grid V061 [Data set]. Accessed 2022-03-05 from. NASA EOSDIS Land Processes DAAC.  
520 <https://doi.org/10.5067/MODIS/MCD19A2.061>, 2022.

521 Marsz, A.A., Matuszko, D. and Styszyńska, A. [The thermal state of the North Atlantic and macro-  
522 circulation conditions in the Atlantic-European sector, and changes in sunshine duration in Central  
523 Europe. \*Int J Climatol.\* 42, 748 - 761. <https://doi.org/10.1002/joc.7270>, 2021.](https://doi.org/10.1002/joc.7270)

524 Moradi, I.: Quality control of global solar radiation using sunshine duration hours. *Energy*, 34, 1-6.  
525 <https://doi.org/10.1016/J.ENERGY.2008.09.006>, 2009

526 O'Dowd, C. D. and Smith, M. H.: Physicochemical properties of aerosols over the northeast Atlantic:  
527 Evidence for wind-speed-related submicron sea-salt aerosol production. *J. Geophys. Res. Atmos.*, 98(D1),

528 1137-1149. <https://doi.org/10.1029/92JD02302>, 1993.

529 Paulescu, M., Stefu, N., Calinoiu, D., Paulescu, E., Pop, N., Boată, R. and Mares, O.: Ångström–Prescott  
530 equation: Physical basis, empirical models and sensitivity analysis. *Renew. Sust. Energ. Rev.*, 62, 495-  
531 506. <https://doi.org/10.1016/J.RSER.2016.04.012>, 2016.

532 Qin, S., Liu, Z., Qiu, R., Luo, Y., Wu, J., Zhang, B., Wu, L. and Agathokleous, E.: Short-term global  
533 solar radiation forecasting based on an improved method for sunshine duration prediction and public  
534 weather forecasts. *Appl. Energy*, 343, 121205. <https://doi.org/10.1016/j.apenergy.2023.121205>, 2023.

535 Ren, J., Lei, X., Zhang, Y., Wang, M., and Xiang, L.: Sunshine duration variability in haihe river basin,  
536 China, during 1966–2015. *Water*, 9(10), 770. <https://doi.org/10.3390/W9100770>, 2017.

537 Rietveld, M. R.: A new method for estimating the regression coefficients in the formula relating solar  
538 radiation to sunshine. *Agric. Meteorol.*, 19(2-3), 243-252. [https://doi.org/10.1016/0002-1571\(78\)90014-](https://doi.org/10.1016/0002-1571(78)90014-6)  
539 [6](https://doi.org/10.1016/0002-1571(78)90014-6), 1978.

540 Sawada, Y., Okamoto, K., Kunii, M. and Miyoshi, T.: Assimilating Every-10-minute Himawari-8  
541 Infrared Radiances to Improve Convective Predictability. *J. Geophys. Res. Atmos.*, 124, 2546 - 2561.  
542 <https://doi.org/10.1029/2018JD029643>, 2019.

543 Tana, G., Ri, X., Shi, C., Ma, R., Letu, H., Xu, J. and Shi, J.: Retrieval of cloud microphysical properties  
544 from Himawari-8/AHI infrared channels and its application in surface shortwave downward radiation  
545 estimation in the sun glint region. *Remote Sens Environ.*, 290, 113548.  
546 <https://doi.org/10.1016/j.rse.2023.113548>, 2023.

547 Tang, C., Zhu, Y., Wei, Y., Zhao, F., Wu, X. and Tian, X.: Spatiotemporal characteristics and influencing  
548 factors of sunshine duration in China from 1970 to 2019. *Atmosphere*, 13(12), 2015.  
549 <https://doi.org/10.3390/atmos13122015>, 2022.

550 Tang, W., Yang, K., He, J. and Qin, J.: Quality control and estimation of global solar radiation in China.  
551 *Solar Energy*, 84, 466-475. <https://doi.org/10.1016/J.SOLENER.2010.01.006>, 2010.

552 Vivar, M., Fuentes, M., Norton, M., Makrides, G. and Bustamante, I.D.: Estimation of sunshine duration  
553 from the global irradiance measured by a photovoltaic silicon solar cell. *Renew. Sust. Energ. Rev.*, 36,  
554 26-33. <https://doi.org/10.1016/J.RSER.2014.04.045>, 2014.

555 Wang, Y. W., Yang, Y. H., Zhou, X. Y., Zhao, N. and Zhang, J. H.: Air pollution is pushing wind speed  
556 into a regulator of surface solar irradiance in China. *Environ. Res. Lett.*, 9(5), 054004.  
557 <https://doi.org/10.1088/1748-9326/9/5/054004>, 2014.

558 Wu, G., Liu, Y. and Wang, T.: Methods and strategy for modeling daily global solar radiation with  
559 measured meteorological data—A case study in Nanchang station, China. *Energy Convers. Manage.*, 48(9),  
560 2447-2452. <https://doi.org/10.1016/J.ENCONMAN.2007.04.011>, 2007.

561 Xia, X.: Spatiotemporal changes in sunshine duration and cloud amount as well as their relationship in  
562 China during 1954–2005. *J. Geophys. Res. Atmos.*, 115(D7). <https://doi.org/10.1029/2009JD012879>,  
563 2010.

564 Xiong, J., Wang, Z., Lai, C., Liao, Y. and Wu, X.: Spatiotemporal variability of sunshine duration and  
565 influential climatic factors in mainland China during 1959–2017. *Int. J. Climatol.*, 40, 6282 - 6300.  
566 <https://doi.org/10.1002/joc.6580>, 2020.

567 Yao, W., Zhang, C., Wang, X., Zhang, Z., Li, X. and Di, H.: A new correlation between global solar  
568 radiation and the quality of sunshine duration in China. *Energy Convers. Manage.*, 164, 579-587.  
569 <https://doi.org/10.1016/J.ENCONMAN.2018.03.037>, 2018.

570 Yu, L., Zhang, M., Wang, L., Qin, W., Jiang, D. and Li, J.: Variability of surface solar radiation under  
571 clear skies over Qinghai-Tibet Plateau: Role of aerosols and water vapor. *Atmos. Environ.*, 287, 119286,

572 <https://doi.org/10.1016/j.atmosenv.2022.119286>, 2022.

573 Yu, Y., Shi, J., Wang, T., Letu, H., Yuan, P., Zhou, W. and Hu, L.: Evaluation of the Himawari-8  
574 Shortwave Downward Radiation (SWDR) Product and its Comparison With the CERES-SYN, MERRA-  
575 2, and ERA-Interim Datasets. *IEEE J Sel Top Appl Earth Obs Remote Sens*, 12, 519-532.  
576 <https://doi.org/10.1109/JSTARS.2018.2851965>, 2019.

577 Zhang, J., Zhao, L., Deng, S., Xu, W. and Zhang, Y.: A critical review of the models used to estimate  
578 solar radiation. *Renew. Sust. Energ. Rev.*, 70, 314-329. <https://doi.org/10.1016/J.RSER.2016.11.124>,  
579 2017.

580 Zhang, P., Guo, Q., Chen, B. and Feng, X.: The Chinese Next-Generation Geostationary Meteorological  
581 Satellite FY-4 Compared with the Japanese Himawari-8/9 Satellites. *Adv. Meteorol. Sci. Technol.*, (1), 4.  
582 <https://doi.org/10.3969/j.issn.2095-1973.2016.01.010>, 2016. (in chinese)

583 Zhang, X., Liang, S., Wild, M. and Jiang, B.: Analysis of surface incident shortwave radiation from four  
584 satellite products. *Remote Sens Environ.*, 165, 186-202. <https://doi.org/10.1016/J.RSE.2015.05.015>,  
585 2015.

586 Zhang, Z., Fang, S. and Han, J.: A daily sunshine duration (SD) dataset in China from Himawari AHI  
587 imagery (2016-2023) (V2), <https://doi.org/10.57760/sciencedb.10276>, 2024.

588 Zhou, Y., Yu, D., Yang, Q., Pan, S., Gai, Y., Cheng, W., Liu, X. and Tang, S.: Variations of Water  
589 Transparency and Impact Factors in the Bohai and Yellow Seas from Satellite Observations. *Remote*.  
590 *Sens.*, 13, 514. <https://doi.org/10.3390/rs13030514>, 2021.